Microporous and Mesoporous Materials 374 (2024) 113159

Contents lists available at ScienceDirect

Microporous and Mesoporous Materials

journal homepage: www.elsevier.com/locate/micromeso

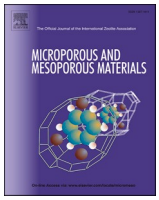

Understanding adsorption mechanisms and metal ion selectivity of superparamagnetic beads with mesoporous CMK-3 carbon and commercial activated carbon

Lisandra de Castro-Alves [a,*], Susana Yáñez-Vilar [a], Manuel A. González-Goméz [a,b], Pelayo Garcia-Acevedo [a], Ángela Arnosa-Prieto [a], Yolanda Piñeiro-Redondo [a,**], José Rivas [a]

[a] Nanotechnology and Magnetism Lab — NANOMAG, Materials Institute – iMATUS, Health Research Institute - IDIS, Department of Applied Physics, Universidad de Santiago de Compostela, E-15782, Santiago de Compostela, Spain
[b] Nanostructured Materials Group, International Iberian Nanotechnology Laboratory-INL, Av. Mestre José Veiga s/n, 4715-330, Braga, Portugal

ARTICLE INFO

Keywords:
Heavy metals
Adsorption
Sodium alginate
Multimetal
Water
CMK-3 mesoporous carbon

ABSTRACT

This study investigates, the adsorption capacities of synthesized magnetic hybrid beads containing ordered mesoporous carbon (CMK-3) and commercial activated carbon (commercial AC) for Cd (II), Ni (II), and Hg (II) ions adsorption in single and ternary systems. The order of maximum adsorption capacity was Cd (II) > Ni (II) > Hg (II) in both beads and systems. L13 beads containing CMK-3 exhibit superior adsorption efficiency compared to L3 beads with commercial AC, attributed to the large surface area, enhanced accessibility to adsorption sites, and the presence of O=C bonds, as well as other elements such as F^-. Adsorption of all metal ions was described by Freundlich isotherm in L3 beads in both systems, meanwhile in L13 beads, Langmuir and Freundlich models described adsorption differently in both systems and among metal ions, indicating a more complex process. According to the reported maximum adsorption capacity values, L3 beads exhibit a greater affinity for Hg (II) ions, while L13 beads show a higher affinity for Cd (II) and Ni (II) ions. Adsorption in both beads occurred through several mechanisms involving surface complexation, ion-exchange, precipitation, physical and chemical processes. These findings highlight the importance of material design in optimizing adsorption performance for environmental applications, with potential for further enhancement of adsorption capacities and selectivities through future research.

1. Introduction

The contamination of environmental systems by heavy metals such as mercury, cadmium, and other metal ions poses a significant environmental challenge. Elevated concentrations of these heavy metals induce toxic effects and lead to their accumulation within the food chain, thereby impacting aquatic ecosystems and posing risks to human health. Consequently, effective remediation strategies are essential for the removal of these pollutants from water. Recent efforts have focused on the development of cost-effective and highly efficient adsorbents, including activated carbon [1], polymers [2–5], and aluminosilicates [6], due to their cost-efficiency, versatility, and efficacy [7].

Activated carbon, characterized by its prevalent microporous structure with pore sizes typically below 10 nm, is a widely recognized and extensively utilized adsorbent. However, alternative carbon-based materials such as carbon nanotubes, carbon aerogels, and ordered mesoporous carbon have garnered significant interest over time [8].

Ordered mesoporous carbons (OMCs) can be synthesized through two main routes: “hard-templating,” which involves the carbonization of a template, and “soft-templating,” a simpler one-step method utilizing triblock copolymers as templates [9]. OMCs exhibit chemical inertness, robust mechanical strength, thermal stability, an ordered pore structure, and a hydrophobic surface, facilitating the effective adsorption of long-chain organic molecules [10]. In recent years, CMK-3, a specific type of OMC, has widespread application in adsorption [11–13] and catalysis [12], including CO_2 adsorption from industrial coal ash [14] and the removal of NOx at low temperatures [15]. Nevertheless, CMK-3 and powdered materials used as adsorbents suffer from drawbacks such

* Corresponding author.
** Corresponding author.
E-mail addresses: lisandracristina.decastro@usc.es (L. de Castro-Alves), y.pineiro.redondo@usc.es (Y. Piñeiro-Redondo).

https://doi.org/10.1016/j.micromeso.2024.113159
Received 13 March 2024; Received in revised form 16 April 2024; Accepted 1 May 2024
Available online 3 May 2024

as particle size, low mechanical strength, and difficulties in separation from aqueous matrices [16]. These challenges can be mitigated through the immobilization of adsorbents onto porous natural polymers, enhancing characteristics such as porosity, rigidity, ease of separation, and mechanical strength.

Alginate, a naturally occurring polysaccharide derived from brown algae, is a versatile biopolymer utilized as an immobilization matrix due to its inexpensive production, non-toxic nature, and biodegradability [17]. Numerous alginate-based adsorbents exhibit high affinity and binding capacities for metal ions in aqueous solutions, primarily attributed to the abundance of carboxylic and hydroxyl functional groups [18]. However, the separation of alginate-loaded materials presents a challenge. Thus, a novel strategy involves incorporating magnetite nanoparticles (Fe_3O_4 NPs) into a polymer matrix such as sodium alginate, resulting in hybrid magnetic beads. This approach offers an effective and rapid means of magnetic separation following the removal of metal ions from water [19–21].

The removal of heavy metals from mixed systems is crucial as wastewater often contains multiple metals, leading to competition for adsorption sites. Investigating adsorption interactions among different metals within mixed systems is vital for predicting metal adsorption in realistic scenarios and optimizing experimental studies. Various isotherm models are employed to elucidate and analyze the adsorption of contaminant systems at equilibrium [22,23]. The Langmuir and Freundlich isotherm models are commonly used to predict the adsorbed material's quantity as a function of concentration at constant temperature [24]. Usually, the mentioned adsorption models are solved by linearization, and the linear regression coefficient (R^2) close to unit is used as indicative of best fittingness of the model. Nevertheless, transformation of the nonlinear equations into their linear form can lead to errors, and potentially violate the assumptions of standard least squares [25]. Recently, more investigations are relaying on the nonlinear method since it proved to give better fitting results than the linear method for isotherm models [26,27].

This research aimed to study the adsorption capacity of magnetic alginate beads incorporating CMK-3 mesoporous carbon and commercial activated carbon (commercial AC) for the removal of metal ions from mixed solutions. The physicochemical properties of both beads and carbons were fully studied to understand the metal ions selectivity and adsorption mechanisms in the ternary system. Besides this, it was determined the best fitting relationship between adsorbate and adsorbent based on error calculation between the experimental and predicted equilibrium adsorption data of the linear and nonlinear isotherm models of Langmuir, Freundlich, Dubinin-Kaganer-Radushkevich (DKR), and Temkin. The developed magnetic alginate beads offer a practical solution for the removal of heavy metal ions from mixed solutions, with potential implications for enhancing water purification and environmental remediation efforts.

2. Materials and methods

2.1. Materials

All chemicals used were of analytical grade and without purification. Ferric chloride ($FeCl_3{\cdot}6H_2O$) was obtained from Alfa Aesar (Madrid, Spain), cadmium chloride hemi(pentahydrate) ($CdCl_2{\cdot}2.5H_2O$, 99 %), and mercury (II) chloride ($HgCl_2$, 99.5 %), from Acros Organics (Geel, Belgium), nickel (II) chloride hexahydrate ($NiCl_2{\cdot}6H_2O$, 99.9 5 %) from Alfa Aesar, (Kandel, Germany), surfactant Tween 20 from Fluka (Steinheim, Germany), commercial activated carbon powder (MW = 12.01 g) was obtained from PANREAC (Madrid, Spain), ferrous sulfate ($FeSO_4{\cdot}7H_2O$), calcium chloride ($CaCl_2$), ammonium hydroxide (NH_4OH, 28 %), triblock copolymer Pluronic P123 (PEO20-PPO70-PEO20), tetraethyl orthosilicate (TEOS, 98 %), sucrose (99 %), sulphuric acid (H_2SO_4, 95–97 %), Hydrofluoric acid (HF, 48 %), hydrochloric acid (HCl, 37 %), and sodium alginate were purchased from Sigma Aldrich (Saint Louis, MO, USA).

2.2. Synthesis of mesoporous silica (SBA-15) and mesoporous carbon (CMK-3)

SBA-15, was prepared according to the procedure described by Zhao et al. [28] with some modifications, using triblock copolymer, P123 as the surfactant, and TEOS as the silica source. Typically, 4.0 g of P123 were dissolved in 150 mL of HCl (1.6 M) at 35 °C for 3 h. Posteriorly, 8.5 g of TEOS was added dropwise under vigorous stirring (500 rpm) for 20 h at 35 °C. The resultant white precipitated was aged at 80 °C for 20 h without agitation. The sample was filtered, washed abundantly with water, and calcined at heating rate of 1 °C/min to a temperature of 500 °C for 6 h, and cool down at a rate of 3 °C/min.

CMK-3, was synthesized using SBA-15 as hard template impregnated with a sucrose solution, according to previous work [29]. Briefly, 1.0 g of SBA-15 was added to a previously prepared solution of 1.25 g of sucrose, and 0.14 g of H_2SO_4 in 5.0 g of H_2O. The mixture was place in a drying oven for 6 h at 100 °C (1 °C/min), and subsequently to 160 °C for 6 h (1 °C/min), after that it was cold down at a rate of 25 °C/min. The sample was treated again at 100 °C and 160 °C with the temperature rates, after the addition of 0.8 g of sucrose, 0.09 g of H_2SO_4 in 5.0 g of H_2O. The sucrose-SBA-15 sample was then carbonized under nitrogen flow with a heating rate of 2 °C/min to 500 °C and then 5 °C/min to 900 °C for 6 h, cooling down at a rate of 3 °C/min). Afterwards, present silica in the sample was removed using a solution of 10 wt% HF under magnetic agitation for 24h at ambient temperature. The sample was then filtered, washed with water and dried at 120 °C for 12 h.

2.3. Synthesis of magnetic alginate beads

Magnetic alginate beads were prepared by extrusion method of Fe_3O_4 NPs with sodium alginate using calcium chloride as cross-linking agent. Firstly, Fe_3O_4 NPs were synthesized by reverse coprecipitation method [21]. Briefly, 15 mL of 1.0 M $FeCl_3{\cdot}6H_2O$, and 0.5 M $FeSO_4{\cdot}7H_2O$ were mixed. Afterwards, the iron salt solution was added dropwise into a 20 mL of 3.5 M NH_4OH at 60 °C, and mechanically stirred for 30 min. The magnetic nanoparticles were then washed, and re-dispersed in distilled water.

For the beads, 2.0 g of sodium alginate was subsequently added to the previously prepared Fe_3O_4 NPs solution (35 mL). Two sets of magnetic beads were prepared, one with commercial AC, and another with previously prepared, CMK-3 mesoporous carbon. For this, 3.0 g of commercial AC (34.3 wt%), and 0.2 g of CMK-3 (7.69 wt%), were added to sodium alginate/Fe_3O_4 NPs solutions, and mechanically stirred for 4 h. The obtained magnetic solutions were added dropwise into 100 mL coagulation bath of 0.13 M $CaCl_2$ with 450 μl Tween 20 under continuous magnetic agitation (450 rpm) using a New Era NE-300 syringe pump. Beads were instantly formed and left in the bath for 20 min. Afterwards, the beads were cleaned with distilled water, and dried overnight at 60 °C. The beads with commercial AC, and CMK-3 mesoporous carbon, were named as L3 and L13, respectively.

2.4. Adsorption studies

Batch adsorption studies of Cd (II), Ni (II), and Hg (II) were performed to determine the adsorption capacity of the beads in a single and ternary system. Solutions of 15 mL, with initial metal concentration between 10 and 250 mg/L and pH value of 4.5. The effect of the metal ions initial concentration was studied with the following conditions (magnetic agitation of 300 rpm, 14 mg of adsorbent dosage, and a contact time of 6 h). Metal concentration in solution was determined by ICP-OES.

Metal ions removal efficiency was calculated using the following Eq. (1):

$$\%R = \frac{(C_0 - C_e)}{C_0} x\ 100 \quad (1)$$

The equilibrium adsorption capacity, q_e, was determined using Eq. (2):

$$q_e = \frac{(C_0 - C_{eq}) * V}{m} \quad (2)$$

Where, R (%) is the removal efficiency, C_0 (mg/L) is the initial metal concentration, C_e (mg/L) is the equilibrium metal concentration present in solution, V (L) is the volume, m (g) is the adsorbent dry weight [30].

2.5. Adsorption isotherm models

A set of isotherm models have been developed to describe the adsorption phenomena. Langmuir, Freundlich, Temkin, or DKR isotherm models are some of the few that consider distinct characteristics of both the adsorbent material and the adsorbed species.

2.5.1. Langmuir isotherm model

The Langmuir isotherm model assumes a monolayer, and homogeneous adsorption onto a surface. The adsorbent surface contains a finite number of adsorption sites that possess an equal affinity for the adsorbate. Once a site is filled, no further adsorption can occur in that site, indicating surface saturation. The isotherm is expressed by the following non-linear Eq. (3) [23]:

$$q_e = \frac{q_m K_L C_e}{1 + K_L C_e} \quad (3)$$

The linear form of the Langmuir isotherm is given by Eq. (4):

$$\frac{C_e}{q_e} = \frac{1}{K_L q_m} + \frac{C_e}{q_m} \quad (4)$$

where, q_e (mg/g), is the amount adsorbed, C_e (mg/L), is the adsorbate concentration in solution, both at equilibrium, K_L (L/mg), is the Langmuir adsorption constant, and q_m (mg/g), is the maximum adsorption capacity for monolayer formation on the adsorbent. The adsorption equilibrium data was plotted as C_e/q_e against C_e.

2.5.2. Freundlich isotherm model

The Freundlich isotherm assumes that the adsorption takes place on a heterogeneous multilayer surface with no limited degree of adsorption sites, and the energy is non-uniformly distributed. The isotherm is represented by the non-linear Eq. (5) [31]:

$$q_e = K_F C_e^{1/n} \quad (5)$$

The linear form of the Freundlich isotherm is given by Eq. (6):

$$\log q_e = \log K_F + \frac{1}{n} log\ C_e \quad (6)$$

where, K_F and n, indicate the adsorption capacity and the adsorption linearity, respectively. The equilibrium data for the adsorption is plotted as $\log q_e$ against $\log C_e$. The two constants, K_F and n are calculated from the curve. Deviation of n constant from unity indicates a nonlinear adsorption that takes place on heterogeneous surfaces [32]. If n value is equal to unity ($n = 1$), adsorption is linear. If ($n > 1$) adsorption is favourable, and is a physical process. Adsorption is considered to fit the Freundlich approach when exponent n takes values within the range 1–10 [33].

2.5.3. Temkin isotherm model

The Temkin isotherm model assumes that the heat of adsorption (ΔH_{ads}) of adsorbate present in the surface layer decreases linearly as a result of increased surface coverage [34]. Also, the equation reveals a uniform distribution of binding energies. Adsorbed quantity, q_e, was plotted against $ln\ C_e$, and the constants were determined from the slope and intercept. The model is represented by the following non-linear Eq. (7) [35].

$$q_e = \text{btln}(K_T C_e) \quad (7)$$

where, b_T (J/mol), is the constant related to the adsorption heat and K_T (L/g), is the Temkin isotherm equilibrium binding constant. However, is commonly used the rearranged linear form of the Temkin isotherm equation, represented by Eq. (8):

$$q_e = \frac{RT}{b_T} \ln K_T + \frac{RT}{b_T} ln\ C_e \quad (8)$$

where, R, (8.314 J/molK), is the universal gas constant and T (K), is the absolute temperature.

2.5.4. DKR isotherm model

The DKR isotherm model assumes that the adsorption curve depends on the adsorbent's porous structure, and that adsorption adopts a multilayer pore filling character, where electrostatic interactions (*van der Waals* forces) are the main physical forces during the process [36]. The non-linear equation form is expressed as:

$$q_e = q_m \exp\left(-\beta\varepsilon^2\right) \quad (9)$$

where, q_m (mg/g), is the adsorption capacity (maximum theoretical adsorption capacity for the formation of a monolayer). β, is the DKR constant representing mean adsorption energy (mol^2/kJ^2) and ε, is the Polanyi potential, which can be calculated through Eq. (10):

$$\varepsilon = \text{RTln}\left(1 + \frac{1}{C_e}\right) \quad (10)$$

The linear form of this model is described as:

$$\ln q_e = \ln q_m - \beta\varepsilon^2 \quad (11)$$

Furthermore, the E value describes the type of adsorption, if the value is under 1–8 kJ/mol or within 8–16 kJ/mol, the adsorption process is physical (electrostatic interactions) or chemical (covalent interactions), respectively. The value of E can be calculated using Eq. (12) [37]:

$$E = \frac{1}{\sqrt{2\beta}} \quad (12)$$

2.6. Linear and nonlinear isotherm models analysis

Linear regression has been used to verify the theoretical assumptions of various models by the best fitting relationship between adsorbate and adsorbent. The accuracy of the fitting is only assessed by the coefficient of determination (R^2), where the values of R^2 close to unity are considered a best fit. The adsorption isotherm was solved in Origin 2018, and the model's constants were calculated from the slope and intercept of the linear regression curves. However, the transformation of the nonlinear regression to the linear regression of the isotherm models produces bias errors (poor linearity). For this reason, to avoid these errors, the nonlinear regression method was used to determine the adsorption constants. This employed process of using the nonlinear regression instead of the linear regression has been recommended by several researchers [38,39].

The software MATLAB (Math Works Inc. Release r2020b, Perpetual License number 40903113, Universidad de Santiago de Compostela, Spain) was used to fit the experimental data to nonlinear equation models using the function (*lsqcurvefit*), which solves the curve-fitting data in the least-square method. Several error functions were used for isotherm equations. In each case, parameters were determined by minimizing well-known error functions to calculate the error deviation between the experimental and predicted equilibrium adsorption data of

the linear and nonlinear models mentioned above.

The following five statistical error functions were used: Sum of the Square of the Errors (ERRSQ), Composite Fractional Error Function (HYBRID), Derivative of Marquardt's Percent Standard Deviation (MPSD), Sum of the Absolute Errors (EABS), and the Average Relative Error (ARE). In addition, the chi-square test (χ^2) was calculated to measure the fittingness between experimental, and calculated equilibrium adsorption data, using the following Eq. (13):

$$\chi^2 = \sum_{i=1}^{n} \frac{\left(q_{e.exp} - q_{e.\ calc}\right)^2}{q_{e.calc}} \tag{13}$$

where, $n = 5$ corresponding to the initial metal concentrations (10, 70, 150, 200, and 250 mg/L). A significance level of 0.05 was selected since it assumed a 5 % risk of concluding that a difference exists within our experimental data. The tabular chi-square value at confidence level at 0.05 level with $n - 1$ degrees of freedom was 9.488. Only the MSPD error and chi-square were presented on the result Table SI 1–4 for brevity.

2.7. Nanoparticles and beads characterizations

Structural studies were performed by X-ray diffraction (XRD) using a Philips diffractometer (Panalytical, Callo End, UK) with Cu Kα radiation (λ = 1.5406 Å), with a step size of 0.02° and a counting time of 2 s per step from 10° to 80° (2θ). Small-angle X-ray scattering (SAXS) patterns were recorded on a PANalytical X'Pert Powder Empyrean, with a step size of 0.01° and a counting time of 5 s per step from 0.25° to 6° (2θ). The Fourier transform infrared spectra (FT-IR) was recorded on a Varian FT-IR 670 (Varian, Palo Alto, CA, USA) spectrophotometer in the range 400–4000 cm^{-1}. Raman spectrums were obtained from a WITec Raman confocal microscope (model = ALPHA300R+) using 532 nm diode laser excitation with 0.3 s integration and 450 scans. The BET specific surface area and the pore size distribution of the samples were characterized under N_2 adsorption-desorption isotherms at 77 K using BET Micromeritics Gemini 2360 instrument (Micromeritics, GA, USA). The morphology of Fe_3O_4 NPs, carbons, and magnetic beads were characterized by transmission electron microscopy (TEM) using a JEOL JEM-1011 microscope (JEOL, Tokyo, Japan) operating at 100 kV, and by scanning electron microscopy (SEM) analysis using a ZEISS FE-SEM ULTRA Plus (30 kV) microscope (Zeiss, Oberkochen, Germany).Thermogravimetric analyses (TGA) were performed from 50 to 850 °C at 10 °C/min under nitrogen flow (20 mL/min) using a TGA PerkinElmer Pyris 7 (Perkin, Waltham, MA, USA). The composition and chemical bonding present on the samples was analyzed by X-ray photoelectron spectroscopy (XPS) using a Thermo Scientific K-Alpha ESCA instrument equipped with aluminum Kα monochromatized radiation at 1486.6 eV X-ray source. Magnetic properties were evaluated through hysteresis loop measurements using a vibrating sample magnetometer (VSM) (DMS, Massachusetts, USA) at room temperature, employing an applied field ranging from −10,000 to 10,000 Oe. The concentrations of Cd (II), Hg (II), and Ni (II) ions were quantified using inductively coupled plasma optical emission spectrophotometry (ICP-OES) with an emission spectrometer, specifically the PerkinElmer Model Optima 3300 DV (Perkin, Waltham, Massachusetts, USA).

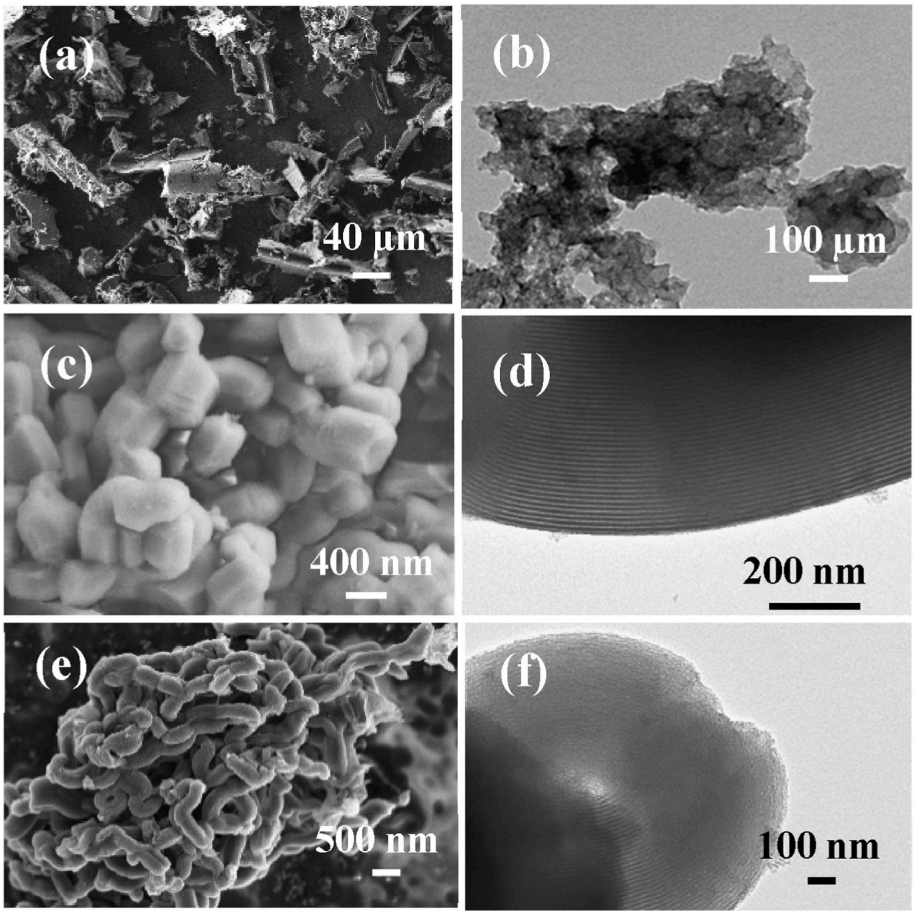

Fig. 1. SEM images of commercial AC (a), SBA-15 (c), and CMK-3 (e) with TEM images of commercial AC (b), SBA-15 (d), and CMK-3 (f), respectively.

3. Results and discussion

3.1. Morphological characterization

The microscopy surface morphology of commercial AC, SBA-15, and CMK-3 mesoporous carbon were studied by SEM and TEM. Fig. 1a and b, show the structure of commercial AC, revealing compact layers with heterogeneous sizes ranging from approximately 40 μm–320 μm.

Mesoporous silica SBA-15, in Fig. 1c, displays a morphological structure of interconnected short bars, which is characteristic of this material. Similarly, in Fig. 1e, the CMK-3 carbon maintains the morphology, and porous structure of its silica precursor. The presence and arrangement of the porous systems in both SBA-15 and CMK-3 was clearly observed, revealing a well-ordered assembly of pores in Fig. 1d and f, respectively.

Fig. 2, shows the SEM micrographs of the external surface and cross-section of the magnetic beads, L3 and L13. Both beads exhibit a spherical morphology, differing significantly in surface, and internal structure. In Fig. 2a, L3 magnetic beads have a porous layer-like surface structure, while, Fig. 2c reveals that the L13 magnetic beads surface features a steep porous valleys indicative of CMK-3 mesoporous carbon. Cross-section SEM images in Fig. 2b and d show the internal architecture of L3 and L13 beads, respectively. Both demonstrate highly porous internal structure, however L3 (Fig. 2b) shows a heterogeneous layer-by-layer arrangement, and manner, L13 (Fig. 2d) consisting of interconnected pores.

3.2. Structural, textural, and microstructural characterization

The structural properties of silica SBA-15, commercial AC, and CMK-3 mesoporous carbon were characterized by SAXS to assess the porous structure and to get more information about nanometer-scale heterogeneities.

Fig. 3a, show diffraction peaks of the precursors used, SBA-15, CMK-3, and commercial AC. The SBA-15 spectra reveal three diffraction peaks at $2\theta = 0.95$, 1.65 and 1.91° that can be indexed to (100), (110) and (200) reflections. This typical pattern of SBA-15 indicates a well-ordered hexagonal mesoporous structure with high degree of symmetry. However, in CMK-3 spectra it is only observed a peak at $2\theta = 0.95°$ indexed to (100) suggesting a less ordered pore structure compared to the SBA-15. Meanwhile, absent diffraction peak in the commercial AC diffractogram indicates that no crystalline phase is present in the sample.

Raman spectra in Fig. 3b, shows two distinctive peaks at 1346 cm^{-1} and 1594 cm^{-1}, which are characteristic of polycrystalline graphite, referred as D peak (disordered induced phonon mode, sp^3), and of a single graphite crystal, which is referred as G peak (graphite lattice mode, E_{2g} sp^2), respectively. The D peak corresponds to the structural defects of carbon during carbonization, while G peak indicates stretching vibration of C–C bonds. The ratio between D and G peaks (I_D/I_G) used to measure the crystalline dimension and in-plane defects in carbon materials was equal to 0.366 in commercial graphite [40]. In this study, the (I_D/I_G) ratio for the CMK-3 and commercial AC was 0.84 and 0.77, respectively, revealing low graphitization degree compared to the commercial graphite value. However, our synthesized CMK-3 carbon (I_D/I_G) value of 0.84 is reportedly lower compared to several studies which reported values higher than 1.0 [41,42].

Commercial AC and CMK-3 carbon were used as precursors for the synthesis of magnetic beads, L3 and L13, respectively. The X-ray diffraction pattern of the beads is shown in Fig. 4a, where five characteristic peaks appearing at $2\theta = 30.1$, 35.8, 43.1, 57.2, and 63.1° can be indexed to (220), (311), (400), (511), and (440) planes corresponding to the magnetite crystalline phase (ICDD: 98-015-8743). The beads chemical topography was analyzed by FTIR spectroscopy as shown in Fig. 4b. Diffraction peaks at 1585 and 1288 cm^{-1} correspond to symmetric and asymmetric C–H stretching vibrations of the carboxyl groups of sodium alginate, respectively. In addition to the broad peak at 3228 cm^{-1} and at 1076 cm^{-1}, which are attributed to the –OH and C–O–C stretching vibrations, respectively [43]. One important band at 558 cm^{-1} was detected, which corresponds to the stretching vibration of Fe–O bonds in Fe_3O_4 NPs [44].

The surface properties of both carbon materials and beads were further investigated by full scan-XPS. Fig. 5a presents the survey scan spectra obtained from the surfaces of commercial AC and CMK-3. In both samples, the carbon (C) signal dominates due to their predominantly carbonaceous nature. Quantitative analysis of the elemental composition revealed atomic percentages of 89.9 % and 91.5 % for carbon in commercial AC and CMK-3, respectively. Additionally, it was also detected as major elements, oxygen (6.8 % and 5.6 %), nitrogen (1.8 % and 0.7 %), and fluor (0.78 % and 1.48 %). Minor elements such as sulfur, phosphorous, and chlorine were also detected, each with atomic percentages lower than 0.5 % for both commercial AC and CMK-3,

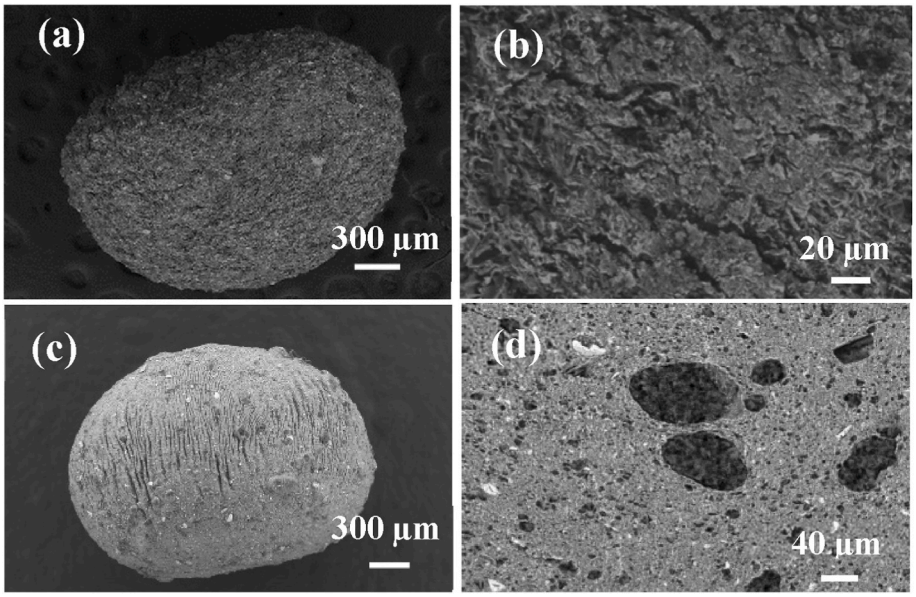

Fig. 2. SEM images of the surface and cross-section structure of L3 (a, b), and L13 (c, d) magnetic beads, respectively.

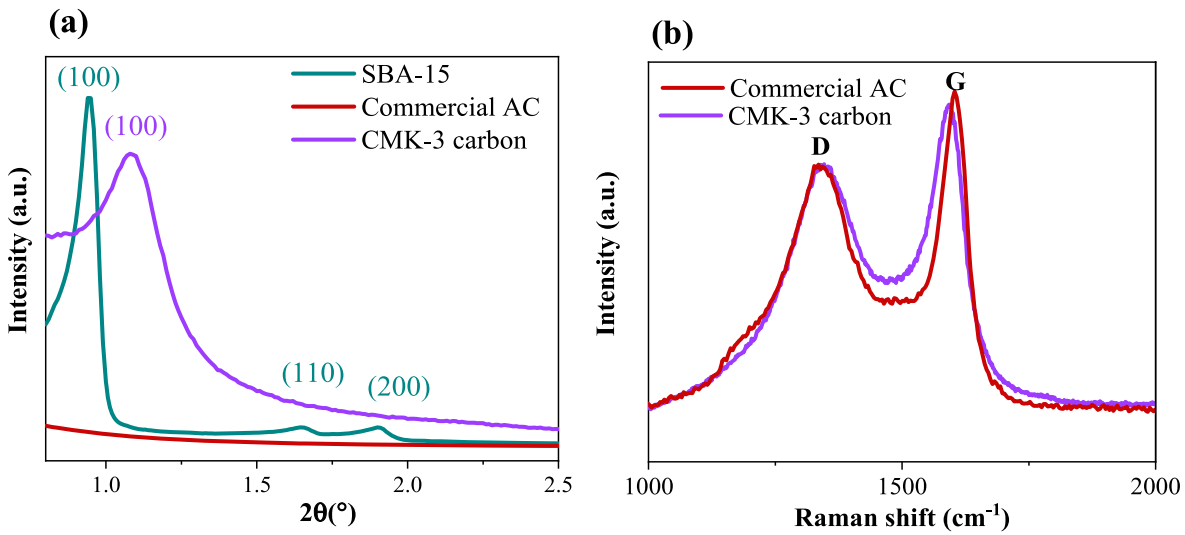

Fig. 3. Small angle X-ray diffraction patterns (a) and Raman spectra (b) of SBA-15, CMK-3 carbon and commercial AC.

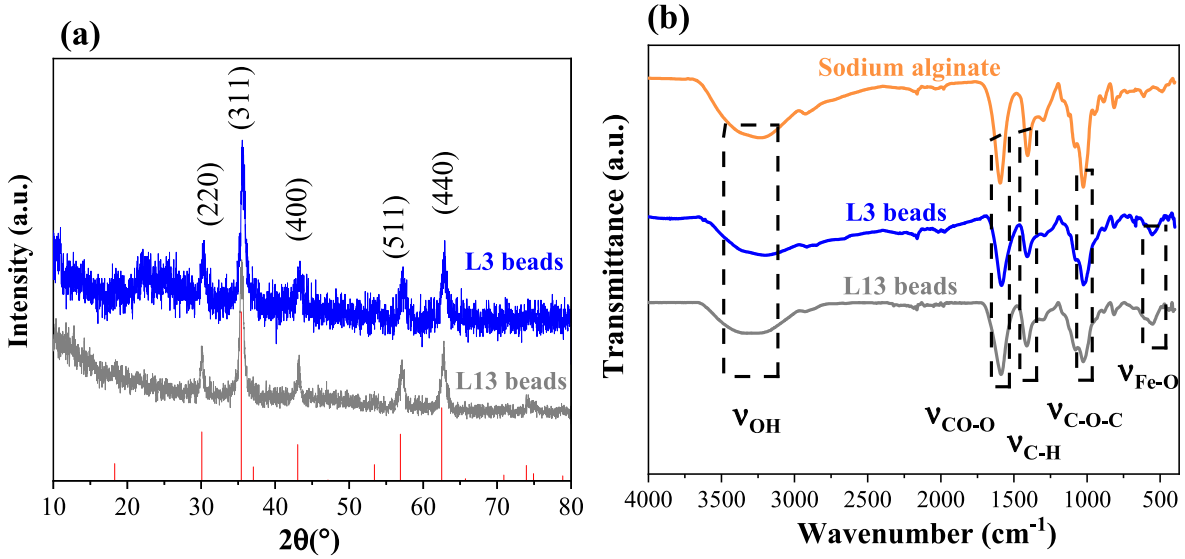

Fig. 4. (a) X-ray diffraction (a) and Infrared spectra (b) of sodium alginate and of the magnetic beads L3 and L13.

respectively.

Fig. 5b presents the survey scan of beads L3 and L13, revealing their elemental composition. Oxygen, carbon, and calcium are identified as major elements, with respective atomic percentages of 35.3 %, 56.2 %, and 2.93 % for L3 beads, and 36.5 %, 57.5 %, and 2.93 % for L13 beads. The presence of calcium, as well as minor elements such as iron and sodium, is attributed to sodium alginate and Fe_3O_4 NPs.

In Fig. 5d, the C 1s peak is deconvoluted into four main peaks for both carbon materials. The strongest peak at 248 eV corresponds to graphitic carbon (C-sp^2), followed by peaks representing the (C–C) bond at 284.8 eV, the (C–O) bond associated with alcohols or ether groups at 286.4 or 286.6 eV, and the (C=O) bond of carbonyl or carboxyl groups at approximately 289 eV. Commercial AC exhibits a higher proportion of (C–C) bonds (18.6 %) compared to CMK-3 (13.1 %), whereas CMK-3 display relatively higher percentages of (C–O) and (C=O) bonds (12.0 % and 5.8 %) compared to commercial AC (10.4 % and 4.9 %), respectively.

Furthermore, the high-resolution C 1s spectra of beads L3 and L13 in Fig. 5d also indicate the presence of (C–C), (C–O), and (C=O) bonds.

L3 beads exhibit the highest percentage of (C–H, 9.5 %) and (C–OH, 18.8 %) bonds, compared to L13 beads, with (C–H, 7.6 %) and (C–OH, 17.1 %). Conversely, the carbonyl bond (C=O) percentage in L13 beads (67.3 %) notably exceeds that of L3 beads (56.8 %).

3.3. Analysis of hysteresis loops

Hysteresis loops of magnetic beads were measured using a vibrating sample magnetometer, which operated within the temperature range of room temperature (−10000 Oe to 10000 Oe). Fig. 6 displays the magnetization curves for Fe_3O_4 NPs, L3, and L13 beads. The magnetization data was subjected to a normalization process relative to the magnetic mass content, determined through TGA. Specifically, the magnetic content percentages were quantified as 86 % for Fe_3O_4 NPs, 23 % for L3 beads, and 43 % for L13 beads. This methodological approach ensures accurate comparison of the magnetic properties of all samples, contributing to a comprehensive understanding of their characteristics.

The saturation magnetization (M_s) values obtained were 59.29 emu/g Fe_3O_4 for Fe_3O_4 NPs, 48.62 and 49.43 emu/g Fe_3O_4 for L3 and L13 beads, respectively. Comparatively, the magnetization of the beads was lower than that of Fe_3O_4 NPs. Notably, negligible coercivity (H_c < 30

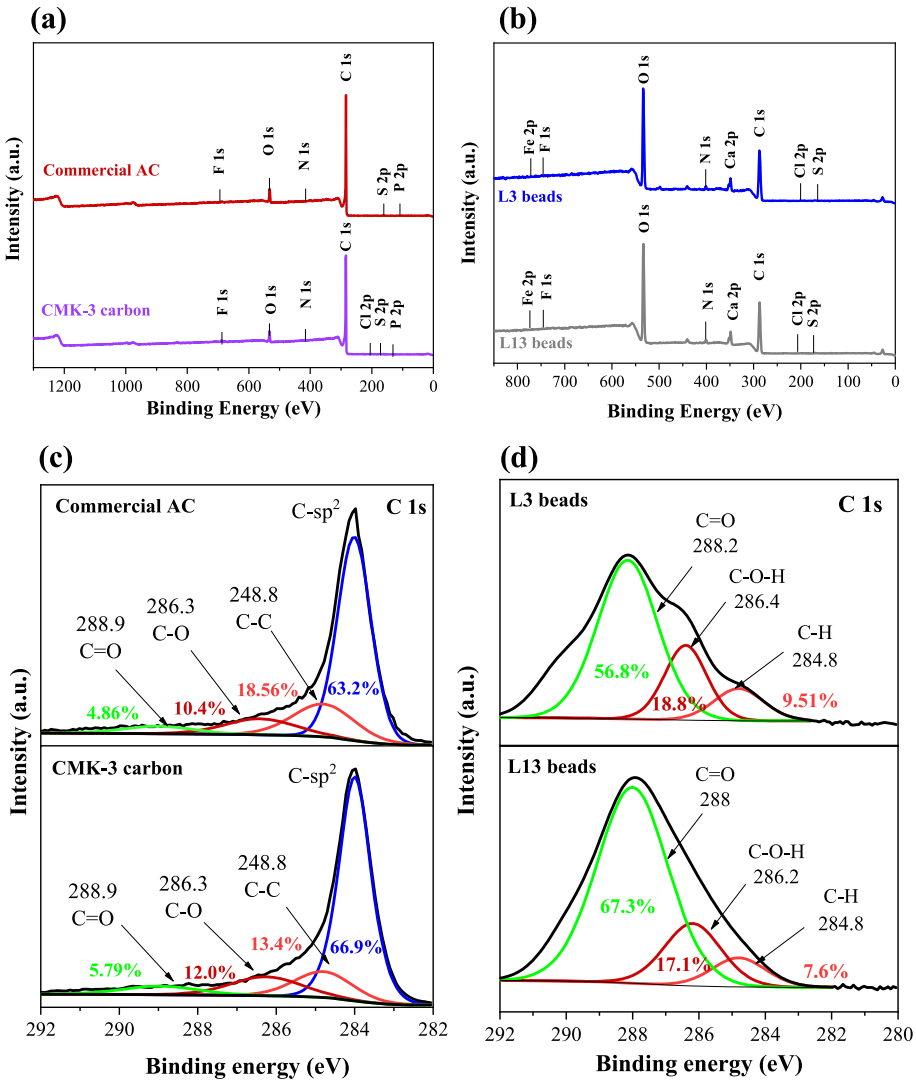

Fig. 5. XPS survey scans (a, b) and deconvolution spectra of the C 1s (c, d) of commercial AC/CMK-3, and of L3/L13 beads, respectively.

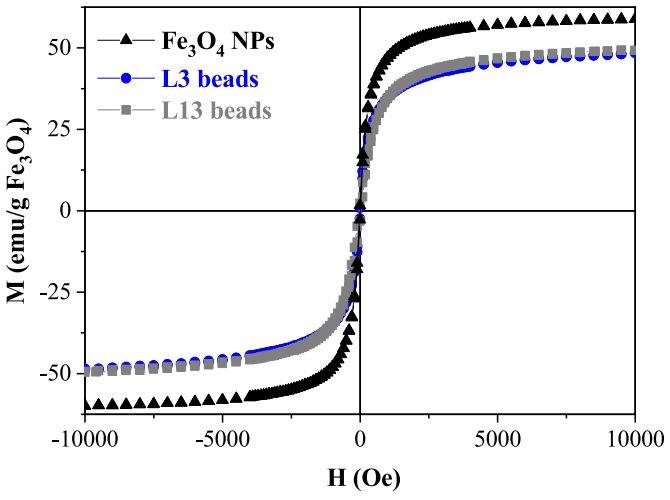

Fig. 6. Magnetic hysteresis loops of Fe_3O_4 NPs, L3, and L13 beads at 25 °C.

Oe) and absent remanence were observed, indicating minimal resistance to changes in the magnetic field strength. This reduction in magnetization aligns with earlier studies, that have observed analogous variations attributing them to the effect of NPs encapsulation by a polymer [21, 45]. However, it is essential to highlight the preservation of the superparamagnetic behavior of Fe_3O_4 NPs within the material. This unique property is an advantage preventing magnetic aggregation and subsequent flocculation in the absence of an external magnetic field. The magnetic material demonstrates remarkable suitability for rapid separation from solutions, providing significant practical utility across diverse industrial applications.

3.4. Surface area and pore volume

Fig. 7 presents a comparative analysis of the N_2 adsorption-desorption isotherm curves obtained for the precursors SBA-15, CMK-3, and commercial AC, along with the magnetic beads L3 and L13. The N_2 adsorption-desorption curve of commercial AC and L3 beads exhibits characteristics of a type II isotherm with a H3 hysteresis loop, as shown in Fig. 7a. This type of isotherm and hysteresis loop is frequently associated with nonporous powders or microporous structures with non-rigid aggregates of plate like-particles. The isotherm curve demonstrates additional adsorption above the relative pressure (p/p_0) of 0.8, which is indicative of interparticle void filling.

Fig. 7b shows the N_2 adsorption isotherm of SBA-15, which has a type IV isotherm with H1 hysteresis, suggesting pore uniformity [18]. Conversely, the CMK-3 carbon and respective L13 bead exhibit a pore

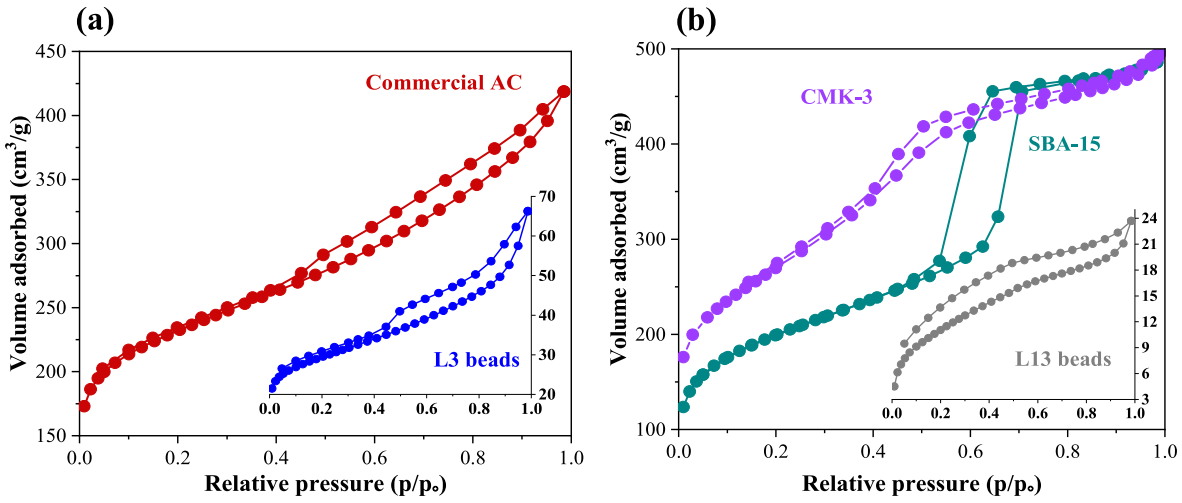

Fig. 7. Nitrogen Adsorption-desorption isotherms of commercial AC/L3 beads (a), and CMK-3/SBA-15/L13 beads (b).

filling step with the relative pressure range (p/p_0) of 0.4–0.8, attributed to mesopores filling. The shape and presence of the hysteresis loop indicate that both CMK-3 and L13 bead have characteristics of a type IV isotherm with an H3 hysteresis loop. The surface areas of SBA-15, CMK-3, and commercial AC were equal to 716, 940, and 849 m^2/g, respectively. CMK-3 carbon had a remarkably higher surface area than SBA-15 and commercial AC, suggesting differences in pore structure, and pore size distribution. Concerning the magnetic beads, L3 beads showed a surface area of 107 m^2/g and L13 of 40.48 m^2/g.

3.5. Adsorption studies

3.5.1. Effect of initial metal concentration

To gain insights into the adsorption capacity of both beads, the influence of initial metal concentration was examined in both single and ternary systems. Aqueous solutions were prepared with initial metal concentrations ranging from 10 to 250 mg/mL, maintaining a pH value of 4.5, which had been previously in another study [20]. The experiments were carried out using 14 mg of adsorbent (L3 and L13 beads)

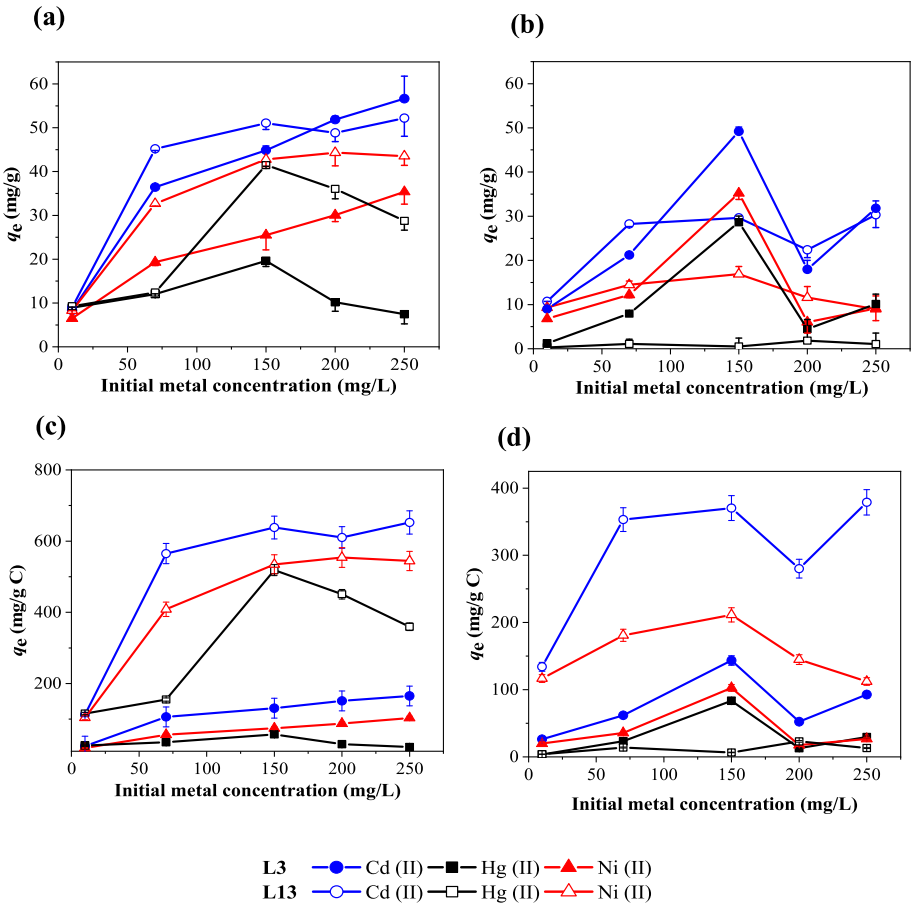

Fig. 8. Adsorption capacity expressed in (mg/g) in the single (a) and ternary system (b) and expressed in (mg/g C) in the single (c) and ternary system (d) of Cd (II), Ni (II) and Hg (II) by L3 and L13 beads.

under magnetic agitation with a stirring velocity of 300 rpm at room temperature. Adsorption capacity was calculated based on the carbon content present in each bead (34.3 % AC commercial in L3 beads and 7.69 % CMK-3 in L13 beads).

Fig. 8 shows the adsorption capacity in (mg/g) and in (mg/g C) of both beads in the single and ternary systems.

Fig. 8a and b show the adsorption capacities (expressed in mg/g) of both beads in the single and ternary systems, respectively. The adsorption capacity values exhibit clear differences in both systems. Specifically, L13 beads demonstrated superior adsorption capacity values for all metal ions compared to the L3 beads in the single system, whereas this trend was reversed in the ternary system. In the single system, L3 beads achieved the highest adsorption capacities, of approximately 55 mg/g for Cd at 250 mg/L, 35 mg/g for Ni at 250 mg/L, and 20 mg/g for Hg at 150 mg/L. Conversely, L13 beads exhibited slightly lower but still notable adsorption capacities, reaching approximately 50 mg/g for Cd at 150 mg/L, 45 mg/g for Ni at 200 mg/L, and 40 mg/g for Hg at 150 mg/L. However, in the ternary system, a decrease in adsorption capacities was observed, as shown in Fig. 8b. The maximum adsorption capacity values for L3 beads were approximately 50 mg/g at 150 mg/L for Cd, 35 mg/g for Ni at 150 mg/L, and 30 mg/g for Hg at 150 mg/L for L3 beads. In contrast, for L13 beads, the corresponding values were approximately 33 mg/g for Cd at 250 mg/L, 25 mg/g for Ni at 150 mg/L, and 3 mg/g for Hg at 200 mg/L. In order to more accurately evaluate the adsorption capacity of the beads relative to the amount of carbon in their composition, the adsorption capacity was calculated by taking into account the percentage of carbon used in both bead types.

Fig. 8c and d show the adsorption capacities (expressed in mg/g C) of both beads in the single and ternary systems, respectively. The adsorption capacity of L13 beads is significantly higher compared to L3 beads, showing a hundredfold increase for all tested metal ions in both single and ternary systems. Consistently, Cd (II) showed the highest adsorption, followed by Ni (II) and Hg (II) in both systems and particle types.

Adsorption of all metal ions was more favored in the single system compared to the ternary system with removal efficiency above 20 % (Supporting information, Fig. S1). In the ternary system, a slight decrease in adsorption capacity suggests a higher competition between metal ions for available binding sites. In the single system, a plateau in Cd (II) and Ni (II) adsorption was observed on the surface of L13 beads due to saturation of adsorption sites, while an increasing trend in Cd (II) and Ni (II) adsorption was observed on L3 beads, indicating ongoing adsorption. Furthermore, the amount of Hg (II) ions adsorbed decreased after reaching maximum adsorption at the initial metal concentration of 150 mg/L in the single system, a phenomenon observed in both bead types. In the ternary system, a maximum adsorption capacity of Cd (II), Ni (II), and Hg (II) at the initial concentration of 150 mg/L was observed only in L3 beads. Equilibrium was achieved faster for Ni (II) and Cd (II) ions compared to Hg (II) ions in L13 beads, whereas no equilibrium was reached in the L3 beads.

The significant difference in adsorption capacity between the two bead types can be attributed to the carbon content in their composition. The mesoporous structure of CMK-3 carbon within L13 beads may have facilitated increased adsorption of metal ions due to the interconnected channels characteristic of the carbon structure. Mesoporous carbons are known for their high specific surface area, large pore volume, and superior adsorption capacity for various contaminants [46,47]. Despite containing only 7.69 wt% CMK-3 compared to 34.3 wt% commercial AC in L3 beads, L13 beads revealed superior adsorption capacity. One reason for this superior adsorption capacity can be attributed to the presence of a higher proportion of mesoporous within L13 beads structure, in contrast, L3 beads were primarily composed of microporous, as observed by the isotherm type determined by BET.

3.5.2. Metal ions competition

In order to assess the competition between metal ions, the chemical states of all metal ions on the beads surface after adsorption in both single and ternary system were evaluated using XPS.

Table 1 shows the binding energies and atomic percentages of Cd, Ni, and Hg in both single and ternary systems for L3 and L13 beads, providing valuable information regarding the chemical states of the metal ions on the bead surfaces under different experimental conditions.

The corresponding binding energies of Cd and Ni elements shifted to lower values from the single to the ternary system at the L3 beads, suggesting competition between the metal ions. In contrast, the mercury peak (Hg 7f7/2) shifted from 101.4 eV in the single system to 101.6 eV in the ternary system, indicating that the adsorption of Hg (II) ions was favored in the presence of Cd (II) and Ni (II) ions.

On the other hand, the observed shifts in binding energies at the L13 bead, from the single to the ternary system, were relatively minor for Cd (406.7 eV–406.8 eV), Hg (101.5 eV–101.6 eV), and Ni (857.4 eV–857.2 eV). This observation led us to believe that L13 beads offered a higher abundance of binding sites available for adsorption to take place in a competitive system.

3.5.3. Linear or nonlinear isotherm models: selection of best model fitting

The experimental data of Cd (II), Hg (II), and Ni (II) ions adsorption by L3 and L13 beads in the single and ternary systems were fitted to the nonlinear and linear Langmuir, Freundlich, Temkin, and DKR models. The calculated parameters are listed in **Table SI** 1–4 and plotted in Figs. 9 and 10. In order to determine the most suitable model for describing the adsorption experimental data, error functions were computed for each model, but only χ^2 errors are displayed in the graphics.

Fig. 9 compares the results obtained from both linear and nonlinear fitting of the experimental data to the Langmuir and Freundlich models. The linear Freundlich model better describes the adsorption of all metal ions by L3 beads in both adsorption systems, evidenced by the low χ^2 values. Notably, lower χ^2 values were observed in the single system compared to the ternary system, which is potentially attributed to the competitive interactions between all metals in the ternary system, as shown in Fig. 9c and d.

Contrarily, the adsorption behavior of metal ions by L13 beads exhibited notable differences between the single and ternary systems. In both systems, the adsorption of some metal ions was described by both

Table 1
Binding energies and atomic percents of elements Cd, Ni, and Hg in the single and ternary system of adsorption by both beads, L3 and L13.

Sample	Element	Peak	Binding energy (eV)		Atomic percent (%)	
			Single syst.	Ternary syst.	Single syst.	Ternary syst.
L3	Cd	Cd 3d3/2	412.7	412.3	0	0
		Cd 3d5/2	405.9	405.6	100	100
	Ni	Ni 2p	861.7	861.9	50.5	48.5
		Ni 2p2/3	856.2	855.9	49.5	51.5
	Hg	Hg 4f5/2	105.3	105.5	0	0
		Hg 4f7/2	101.4	101.6	100	100
L13	Cd	Cd 3d3/2	413.5	413.6	0	0
		Cd 3d5/2	406.7	406.8	100	100
	Ni	Ni 2p	862.5	862.1	41.9	57.8
		Ni 2p2/3	857.4	857.2	58.1	48.3
	Hg	Hg 4f5/2	105.4	105.5	0	0
		Hg 4f7/2	101.5	101.6	100	100

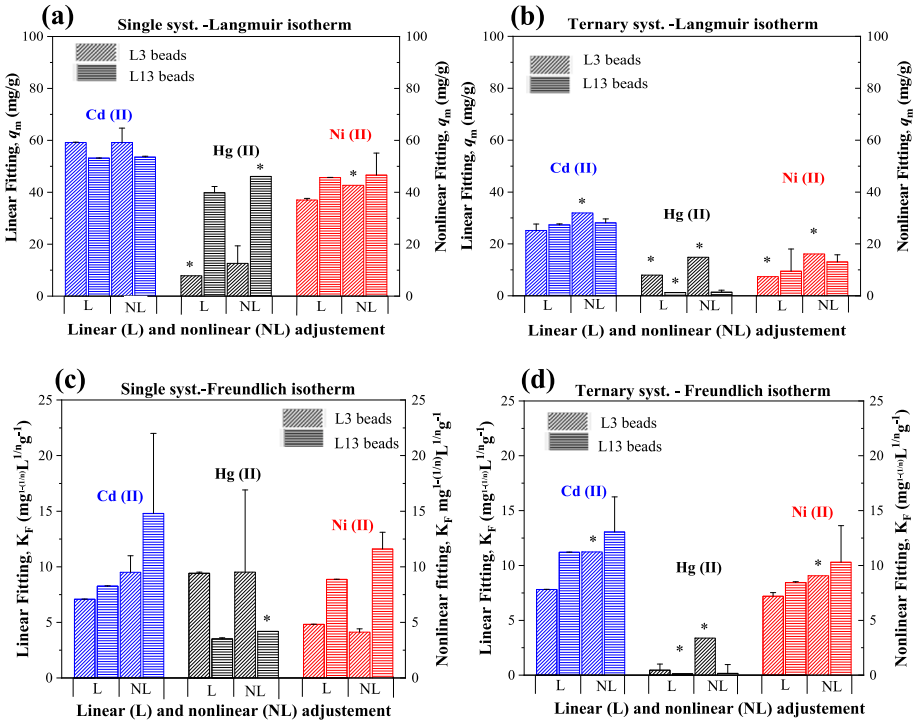

Fig. 9. Linear and nonlinear fitting of Cd (II), Hg (II), and Ni (II) experimental adsorption data at the single and ternary systems by the magnetic beads L3 and L13. Langmuir (a, b) and Freundlich isotherm models fitting (c, d), respectively. (* sign is referred to χ^2 higher than tabular χ^2 of 9.488).

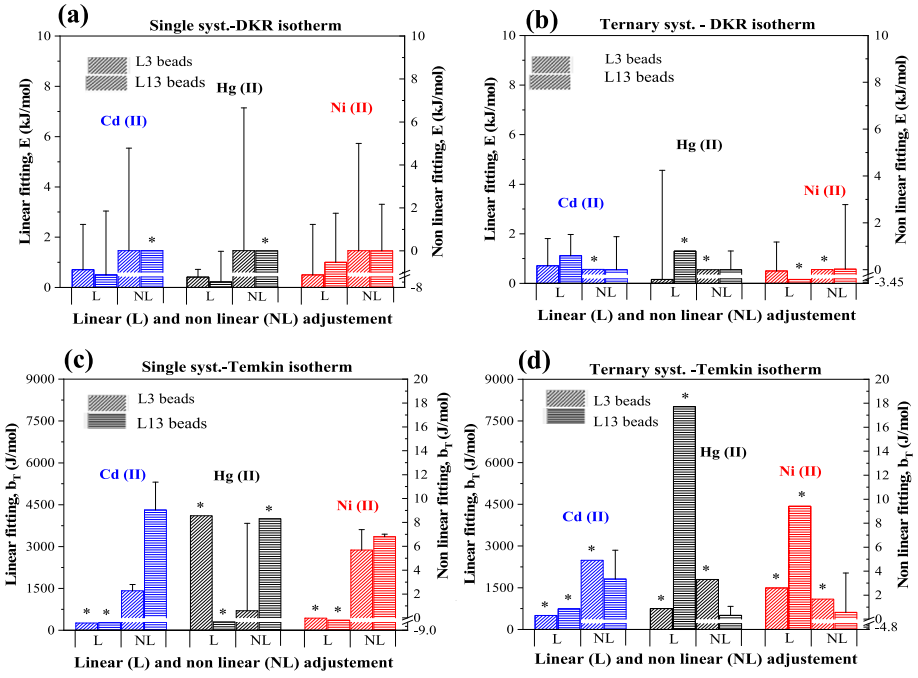

Fig. 10. Linear and nonlinear fitting of Cd (II), Hg (II), and Ni (II) experimental adsorption data at the single and ternary systems by the magnetic beads L3 and L13. DKR (a, b) and Temkin isotherm models fitting (c, d), respectively. (* sign is referred to χ^2 higher than tabular χ^2 of 9.488).

Langmuir and Freundlich isotherm models.

Lower χ^2 error values were computed for Ni (II) and Hg (II) in the linear Freundlich model, while for Cd (II) ions, the linear Langmuir model provided better fit in the single adsorption system, as shown in Fig. 9a and c. In the ternary system, Ni (II) and Cd (II) ions adsorption were better described by the linear Freundlich model, while Hg (II) ions adsorption was better described by both nonlinear Langmuir and nonlinear Freundlich models, as shown in Fig. 9b and d. By observing both Langmuir and Freundlich behavior, it suggests that the adsorption of mercury onto the L13 beads involves both monolayer coverage at specific sites (Langmuir isotherm) and multilayer adsorption onto heterogeneous surfaces with varying affinities (Freundlich isotherm). This analysis highlights the complexity of metal ion adsorption behaviors and the need to consider various adsorption models to accurately describe

and predict their adsorption onto different surfaces under different experimental conditions.

The adsorption capacities of both L3 and L13 beads varied significantly among different metal ions. The adsorption of all metal ions onto the L3 beads, was described by the Freundlich isotherm model. This means that adsorption occurred in a multilayer onto the L3 heterogenous surface with varying distribution and affinity of adsorption sites.

In the single system, the maximum adsorption capacity (K_F, $mg^{1-(1/n)}L^{1/n}g^{-1}$) of L3 beads followed the order Hg (9.43) > Cd (7.09) > Ni (4.82), while in the ternary system, the order was Cd (7.82) > Ni (7.16) > Hg (0.45) (Supporting information, Table S1). Notably, Ni (II) and Cd (II) ions showed higher adsorption in the ternary system, whereas Hg (II) ions displayed the opposite trend.

Meanwhile, metal ion adsorption by L13 beads was described by both Langmuir and Freundlich isotherm models. In the single system, the maximum adsorption capacity $q_m(mg/g)$ of Cd (II) ions by L13 beads was 51.19 mg/g (Supporting information, Table S2) while in the ternary system the Freundlich constant (K_F, $mg^{1-(1/n)}L^{1/n}g^{-1}$) was equal to 11.151. The adsorption of Ni (II) and Hg (II) decreased from the single to the ternary system, as shown by the K_F values of 8.87 and 8.45 for Ni (II), and of 3.51 and 0.17 for Hg (II), respectively. According to the reported maximum adsorption capacity values, it seems that L3 beads exhibit a greater affinity for Hg (II) ions, while L13 beads show a higher affinity for Cd (II) and Ni (II) ions.

Fig. 10 compares the results of linear and nonlinear fitting of the experimental data to the Temkin and DKR models. The linearization of the Temkin model was discarded due to increased χ^2 errors in both beads and systems. The heat release (b_T, J/mol) calculated in nonlinear Temkin model indicated exothermic adsorption for all metal ions since $b_T > 0$ [48]. It was required more binding energy in the ternary system than in single system for Cd (II) and Ni (II) ions adsorption due to the high Temkin binding constant (K_T, L/g) reported. The opposite was observed in Hg (II) ions adsorption by L3 and L13 beads. The DKR model's linearization lowered the χ^2 error except for Hg (II) and Ni (II) ions adsorption in the ternary system. The adsorption energy (E, kJ/mol) was less than 8 kJ/mol in both systems and particles, suggesting that physical forces occurred during adsorption.

The adsorption of all metal ions by L3 beads in both systems, suggests a more consistent adsorption behavior across different metal ions and experimental conditions. This uniformity implies that the adsorption process on L3 beads follows a similar pattern for all metal ions, regardless of whether they are in single or ternary systems.

In contrast, for L13 beads, where both Langmuir and Freundlich models describe the adsorption differently among metal ions and systems (single and ternary), it indicates a more diverse adsorption behavior. This variability suggests that the adsorption process on L13 beads is complexed and influenced by multiple factors, such as surface properties, solution chemistry, and metal ion interactions, leading to different adsorption mechanisms and behaviors for different metal ions and experimental conditions.

The adsorption affinity of L3 beads for Hg (II) ions and L13 beads for Cd (II) and Ni (II) ions was clearly observed. The adsorption affinity of an adsorbent towards metal ions is typically governed by the physicochemical characteristics of the metal species. Previous studies have shown that metals with high molecular weights and ionic radius are generally removed more rapidly than those with lower molecular weight [49,50]. Meanwhile, in other study, metal ions with lower ionic radius were adsorbed more rapidly, while ions with large ionic radius saturate the adsorbent and reduce adsorption efficiency [51].

In our study, the adsorption affinity and capacity of both beads follow the order of Cd (II) > Ni (II) > Hg (II) in both types of beads. The molecular weights of Cd (II), Ni (II), and Hg (II) are 112.41, 58.69, and 200.59 g/mol, respectively. The maximum amount of the studied metal ion adsorbed onto both beads does not follow the trend to increase with the increase of metal ions molecular weight. The adsorption can also be related to the ionic radius of the metal ions. The ionic radius for Cd (II), Ni (II), and Hg (II) are 0.97, 0.69, and 1.02 Å, respectively. The trend observed in this study cannot be correlated with either low or high ionic radius for all metal ions, as observed in several studies. Hg (II) ions with high ionic radius was the least adsorbed of all metal ions in this study, which could be correlated with quick saturation of pores due to its large molecular weight and ionic radius. However, Cd (II) ions with the second highest ionic radius and molecular weight was the most adsorbed metal ion followed by Ni (II) ions.

Concerning hydration energy values, it has been stated that the lower hydration energy, the greater affinity between the ion and functional group of the adsorbent [52]. The hydration energy of Cd (II), Ni (II), and Hg (II) are −1807, −2105, and −1840 kJ/mol, respectively [53,54]. The highest adsorption of Cd (II) ions could be attributed to the low hydration energy compared to Ni (II) and Hg (II) ions. The likelihood of Cd (II) ions bonding to the beads surface is high since lower energy is needed to reduce water molecules in its hydration shell. Therefore, while the hydration free energy may provide some information regarding Cd (II) and Ni (II) ions adsorption, the same does not occur for Hg (II) ions adsorption. A similar adsorption affinity trend (Cd (II) > Ni (II) > Hg (II)) was observed in another study with tetravalent manganese feroxyhyte [55]. In this study, it was observed a better affinity and selectivity of the adsorbent for Cd (II) followed by Ni (II) which was attributed to the lower hydration free energy of Cd (II) and high atomic radius. Meanwhile, the lower affinity for Hg (II) ions was attributed to both high atomic radius and the presence of uncharged species such as $HgCl_2$ or HgOHCl. This highlights the complexity of adsorption processes and in our study, adsorption is not only correlated with hydration free energy alone. Other factors need to be considered, such as chemical properties of the ions and specific interactions between the ions and the beads to understand the observed adsorption trends fully. Further experimental investigation and analysis would be necessary to fully understand the complex relationship between hydration free energy and adsorption capacity.

3.5.4. Adsorption mechanism

The adsorption mechanism can involve several interactions and processes between the adsorbate and the adsorbent. To help us understand the mechanisms involved in the adsorption of Cd (II), Ni (II), Hg (II) ions by L3 and L13 beads, XPS and FTIR analysis were conducted to the beads before and after adsorption.

The XPS results, presented in Table 1, provided insights into the binding energies of all metal ions in both systems. The analysis indicates that Cd is predominantly present in the form of cadmium fluoride (CdF_2), as evidenced by the assigned binding energy of 405.80 eV. Similarly, the binding energy of Ni, observed at 855.75 eV (L3 beads) and 856.12 eV (L13 beads), suggests the presence of nickel hydroxide ($Ni(OH)_2$). For Hg, two peaks are observed at 101.5–105.5 eV (L3 beads) and 101.35–105.25 eV (L13 beads), corresponding to Hg 4f7/2 and 4f5/2, respectively, indicating the adsorbed Hg may exist in the form of $HgCl_2$, HgS_2, or HgO. The XPS does not determine these chemical states because the binding energies overlap in the region of ~101.5 eV. Based on these results, the adsorption mechanism for Ni likely involves coordination and electrostatic interactions, possibly leading to the formation of $Ni(OH)_2$ precipitates. On the other hand, for Cd, the mechanism involved was precipitation, since Cd ions reacted with fluoride (F^-) ions present in both beads and potentially facilitated the formation of CdF_2 complexes or precipitates when in contact with Cd (II) in solution. Since Hg can exist in three forms: $HgCl_2$, HgS_2, or HgO a complex adsorption mechanism involving a combination of surface complexation, chemical bonding, precipitation, and physical adsorption processes. The lower adsorption of Hg (II) ions by both beads can be correlated as previously stated by its presence as uncharged specie of $HgCl_2$ or by its high atomic radius.

To fully understand the adsorption mechanism occurring, FTIR was conducted to elucidate the chemical interactions and identify functional groups on the beads that play a crucial role on the metal's ions

adsorption.

Fig. 11a and b show the spectra of L3 and L13 beads after adsorption in the single and ternary systems, respectively. Following adsorption, a reduction in the intensity of vibrational peaks corresponding to C=O, C–O, and Fe–O bonds was observed. The formation of new bonds occurred during adsorption, leading to a decrease in the COOH bond content within the beads.

Notably, both beads exhibited slight shifts and increased peak intensities after Hg (II) ions adsorption, suggesting structural modifications with the formation of molecular bonds during Hg (II) adsorption [56].

The most significant shifts in bonds of C–O and C=O were observed in L13 beads after adsorption. Specifically, the peak corresponding to C–O shifted from 1017 cm^{-1} to 1022-1027 cm^{-1}, while the C=O peak shifted from 1587 cm^{-1} to 1579-1583 cm^{-1}, indicating their involvement in adsorption at the L13 beads. In both beads, the peak intensity of these bonds was highly reduced after adsorption of Cd (II) and Ni (II) ions, further corroborating their role in adsorption.

Additionally, the stretching vibration of Fe–O in Fe_3O_4 NPs at L3 and L13 beads was detected around 552 and 554 cm^{-1}, respectively. Post-adsorption, the intensity of this bond was diminished, suggesting some displacement of oxygen groups.

XPS analysis in Fig. 11c and d show the deconvoluted peaks of oxygen, the predominant element on the L3 and L13 beads surface, respectively.

The high-resolution spectra of O 1s in both L3 and L13 beads were divided into two peaks corresponding to O=C and O–C bonds. A shift of the O 1s peaks towards lower binding energies was observed in both beads in the ternary system. This is an indication of new bond formation between metal ions and oxygen groups present on the bead surfaces. Specifically, a new bond between oxygen and metal ions was observed at 530.3 eV and 530.9 eV with atomic percentages of 11.1 % and 7.9 % for

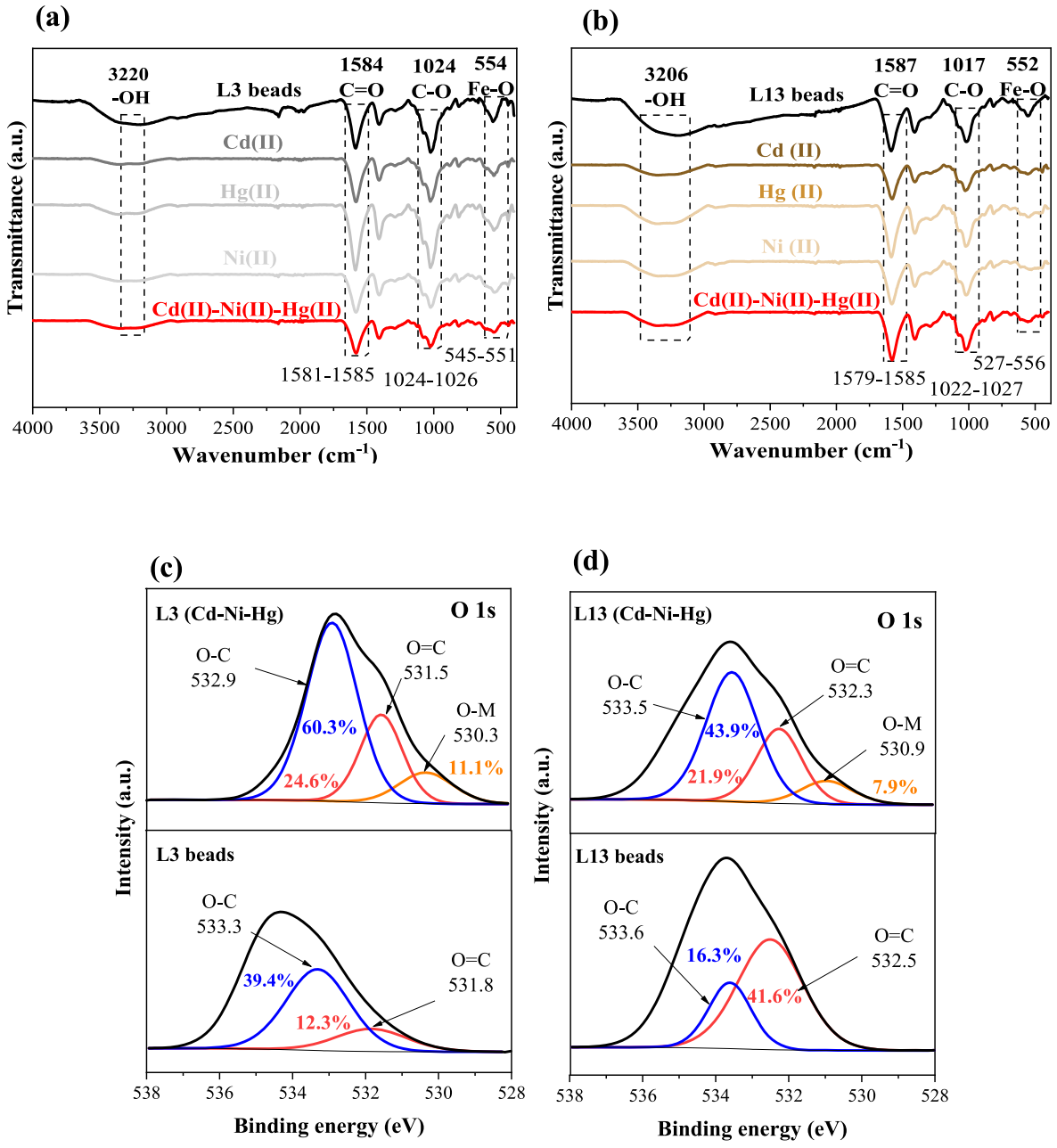

Fig. 11. FTIR spectra before and after metal ions adsorption by L3 (a) and L13 (b) at the single, and ternary system. XPS high resolution spectra of O 1s in L3 (c) and L13 (d) beads, before and after adsorption at the ternary system.

L3 and L13 beads, respectively.

In L3 beads, the atomic percentages increased from 12.3 % to 39.4 %–24.6 % and 60.3 % for O=C and O–C bonds, respectively. Conversely, in L13 beads, the O=C bond's relative percentage decreased from 41.6 % to 21.9 %, while the O–C bond increased from 16.3 % to 43.9 %. This suggests that at L13 beads, C=O double bonds rupture and were converted into single O–C or M − O bonds post-adsorption. Additionally, the ratio of O=C/O–C at L3 beads increased from 0.31 % to 0.41 %, and in the L13 beads decreased from 2.6 % to 0.49 %. These findings imply that while O=C bonds served as one of the routes for metal ions adsorption in both beads, this phenomenon was more pronounced in the L13 beads.

Adsorption is complex, and several mechanisms occurred simultaneous in our study, as shown in Scheme 1. Surface complexation, chemical bonding, precipitation and physical adsorption processes occurred with several elements and functional groups present on the beads. However, the high adsorption ability of the L13 beads compared to the L3 beads, can be attributed to several factors. Firstly, L13 beads contained mesoporous carbon CMK-3, which provided a larger surface area and more accessible adsorption sites compared to the L3 beads with commercial AC. This increase surface area and pore structure of L13 beads likely enhanced the adsorption capacity for Cd (II) and Ni (II) ions, and lastly Hg (II). It is believed that Cd (II) and Ni (II) were adsorbed first due to the higher abundance of pore sites with O=C groups and other elements such as F^- (derived from HF used in the CMK-3 synthesis). The adsorption mechanism in L13 beads likely involved a combination of monolayer adsorption on specific sites and multilayer adsorption on the heterogeneous surface, reflecting the diverse nature of the L13 beads.

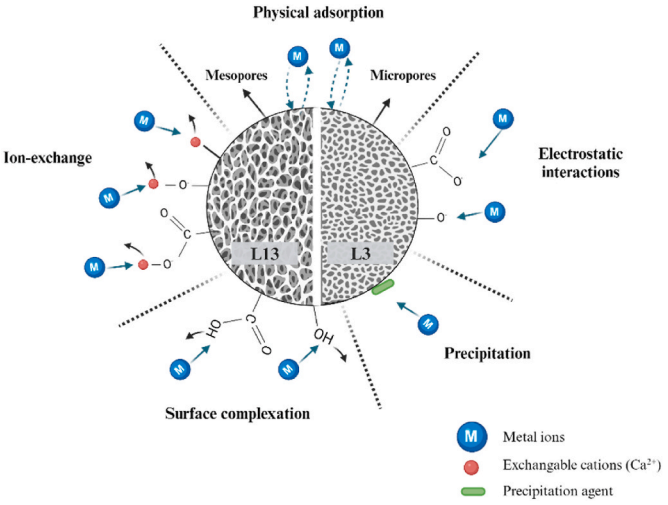

Scheme 1. Schematic representation of the possible adsorption mechanisms occurring at L3 and L13 beads.

4. Conclusions

Synthesized magnetic hybrid beads containing active and mesoporous carbon were characterized and investigated as adsorbents for Cd (II), Ni (II), and Hg (II) adsorption in both single and ternary systems. The maximum adsorption capacity was found to increase in the order of Cd (II) > Ni (II) > Hg (II) in both systems and magnetic beads. Additionally, there were variations in metal ion affinity and adsorption capacity between the two types of magnetic beads. The L13 beads, composed of CMK-3 mesoporous carbon (7.69 wt%), demonstrated superior adsorption efficiency compared to the L3 beads with commercial AC (34.3 wt%). The superior adsorption ability of L13 beads compared to L3 beads can be attributed to a combination of factors. Firstly, the incorporation of mesoporous carbon CMK-3 in L13 beads provided a significantly larger surface area and more accessible adsorption sites, enhancing their capacity for Cd (II), Ni (II) ions, and Hg (II). This increased surface area and unique pore structure likely facilitated the adsorption process by providing abundant active sites for interaction with the target ions. Furthermore, the presence of pore sites rich in functional groups such as O=C and elements like F^- derived from the CMK-3 synthesis process contributed to the preferential adsorption of Cd (II) and Ni (II) ions. Meanwhile, the presence of the commercial AC in L3 beads enhanced its adsorption and selectivity for Hg (II) ions. The adsorption mechanism in L13 beads appears to involve a combination of monolayer adsorption (Langmuir isotherm) on specific sites and multilayer adsorption (Freundlich isotherm) on the heterogeneous surface, highlighting the complexity of the adsorption mechanisms occurring (surface complexation, ion exchange, chemical bonding, precipitation, and physical adsorption). L3 beads demonstrate consistent adsorption behavior across the various metal ions and systems (Freundlich isotherm).

These findings not only deepen our understanding of the adsorption behavior of different bead compositions but also emphasize the importance of material design in optimizing adsorption performance. The insights gained from this study serve as a way for the development of more efficient adsorbents for environmental remediation and wastewater treatment applications. Further research in this direction could focus on exploring additional factors influencing adsorption behavior and optimizing bead composition to achieve even higher adsorption capacities and selectivities.

Funding sources

The research leading to these results has received funding mainly from grant PID2020-112626RB-C21 funded by MCIN/AEI/10.13039/501100011033, modalities « Research Challenges» and «Knowledge Generation».

CRediT authorship contribution statement

Lisandra de Castro-Alves: Writing – review & editing, Writing – original draft, Investigation, Data curation, Conceptualization. **Susana Yáñez-Vilar:** Writing – review & editing, Validation, Methodology, Investigation, Data curation. **Manuel A. González-Goméz:** Investigation, Data curation. **Pelayo Garcia-Acevedo:** Investigation, Data curation. **Ángela Arnosa-Prieto:** Investigation, Data curation. **Yolanda Piñeiro-Redondo:** Writing – review & editing, Supervision, Conceptualization. **José Rivas:** Writing – review & editing, Resources, Project administration, Funding acquisition.

Declaration of competing interest

The authors declare that they have no known competing financial interests or personal relationships that could have appeared to influence the work reported in this paper.

Data availability

No data was used for the research described in the article.

Appendix A. Supplementary data

Supplementary data to this article can be found online at https://doi.org/10.1016/j.micromeso.2024.113159.

References

[1] R. Shahrokhi-Shahraki, C. Benally, M.G. El-Din, J. Park, High efficiency removal of heavy metals using tire-derived activated carbon vs commercial activated carbon: insights into the adsorption mechanisms, Chemosphere 264 (2021) 128455, https://doi.org/10.1016/j.chemosphere.2020.128455.

[2] Z. Zia, A. Hartland, M.R. Mucalo, Use of low-cost biopolymers and biopolymeric composite systems for heavy metal removal from water, Int. J. Environ. Sci. Technol. 17 (2020) 4389–4406, https://doi.org/10.1007/s13762-020-02764-3.
[3] S.S. Li, Y.L. Song, H.R. Yang, Q. Da An, Z.Y. Xiao, S.R. Zhai, Modifying alginate beads using polycarboxyl component for enhanced metal ions removal, Int. J. Biol. Macromol. 158 (2020) 493–501, https://doi.org/10.1016/J.IJBIOMAC.2020.05.038.
[4] Y. Zhao, L. Gai, H. Liu, Q. An, Z. Xiao, S. Zhai, Network interior and surface engineering of alginate-based beads using sorption affinity component for enhanced phosphate capture, Int. J. Biol. Macromol. 162 (2020) 301–309, https://doi.org/10.1016/J.IJBIOMAC.2020.06.159.
[5] W. Zhang, H. Deng, L. Xia, L. Shen, C. Zhang, Q. Lu, S. Sun, Semi-interpenetrating polymer networks prepared from castor oil-based waterborne polyurethanes and carboxymethyl chitosan, Carbohydr. Polym. 256 (2021) 117507, https://doi.org/10.1016/J.CARBPOL.2020.117507.
[6] M.A. Salam, M.R. Abukhadra, M. Mostafa, Effective decontamination of As(V), Hg (II), and U(VI) toxic ions from water using novel muscovite/zeolite aluminosilicate composite: adsorption behavior and mechanism, Environ. Sci. Pollut. Res. Int. 27 (2020) 13247–13260, https://doi.org/10.1007/s11356-020-07945-8.
[7] J. Goscianska, M. Marciniak, R. Pietrzak, Mesoporous carbons modified with lanthanum(III) chloride for methyl orange adsorption, Chem. Eng. J. 247 (2014) 258–264, https://doi.org/10.1016/j.cej.2014.03.012.
[8] K.P. Gopinath, D.V.N. Vo, D. Gnana Prakash, A. Adithya Joseph, S. Viswanathan, J. Arun, Environmental applications of carbon-based materials: a review, Environ. Chem. Lett. 19 (2021) 557–582, https://doi.org/10.1007/S10311-020-01084-9/TABLES/9.
[9] D. Gang, Z. Uddin Ahmad, Q. Lian, L. Yao, M.E. Zappi, A review of adsorptive remediation of environmental pollutants from aqueous phase by ordered mesoporous carbon, Chem. Eng. J. 403 (2021) 126286, https://doi.org/10.1016/J.CEJ.2020.126286.
[10] J.-S. Lee, S.H. Joo, R. Ryoo, Synthesis of mesoporous silicas of controlled pore wall thickness and their replication to ordered nanoporous carbons with various pore diameters, J. Am. Chem. Soc. 124 (2002) 1156–1157, https://doi.org/10.1021/ja012333h.
[11] M. Barczak, K. Michalak-Zwierz, K. Gdula, K. Tyszczuk-Rotko, R. Dobrowolski, A. Dąbrowski, Ordered mesoporous carbons as effective sorbents for removal of heavy metal ions, Microporous Mesoporous Mater. 211 (2015) 162–173, https://doi.org/10.1016/j.micromeso.2015.03.010.
[12] Y. Jeong, M. Cui, J. Choi, Y. Lee, J. Kim, Y. Son, J. Khim, Development of modified mesoporous carbon (CMK-3) for improved adsorption of bisphenol-A, Chemosphere 238 (2020), https://doi.org/10.1016/j.chemosphere.2019.124559.
[13] Z. Ezzeddine, I. Batonneau-Gener, Y. Pouilloux, H. Hamad, Removal of methylene blue by mesoporous CMK-3: kinetics, isotherms and thermodynamics, J. Mol. Liq. 223 (2016) 763–770, https://doi.org/10.1016/j.molliq.2016.09.003.
[14] L. Hu, S. Dang, X. Yang, J. Dai, Synthesis of recyclable catalyst–sorbent Fe/CMK-3 for dry oxidation of phenol, Microporous Mesoporous Mater. 147 (2012) 188–193, https://doi.org/10.1016/j.micromeso.2011.06.015.
[15] R. Wu, Q. Ye, K. Wu, S. Cheng, T. Kang, H. Dai, Adsorption performance of CMK-3 and C-FDU-15 in NO removal at low temperature, J. Environ. Sci. (China) 87 (2020) 289–298, https://doi.org/10.1016/j.jes.2019.07.014.
[16] Q.U. Jiuhui, Research progress of novel adsorption processes in water purification: a review, J. Environ. Sci. (China) 20 (2008) 1–13, https://doi.org/10.1016/s1001-0742(08)60001-7.
[17] R. Abka-khajouei, L. Tounsi, N. Shahabi, A.K. Patel, S. Abdelkafi, P. Michaud, Structures, properties and applications of alginates, Mar. Drugs 20 (2022) 364, https://doi.org/10.3390/MD20060364, 20 (2022) 364.
[18] Y. Jeong, M. Cui, J. Choi, Y. Lee, J. Kim, Y. Son, J. Khim, Development of modified mesoporous carbon (CMK-3) for improved adsorption of bisphenol-A, Chemosphere 238 (2020) 124559, https://doi.org/10.1016/j.chemosphere.2019.124559.
[19] K.G. Akpomie, J. Conradie, K.A. Adegoke, K.O. Oyedotun, JoshuaO. Ighalo, J. F. Amaku, C. Olisah, A.O. Adeola, K.O. Iwuozor, Adsorption mechanism and modeling of radionuclides and heavy metals onto ZnO nanoparticles: a review, Appl. Water Sci. 13 (2023) 20, https://doi.org/10.1007/s13201-022-01827-9.
[20] L. de Castro Alves, S. Yáñez-Vilar, Y. Piñeiro-Redondo, J. Rivas, Efficient separation of heavy metals by magnetic nanostructured beads, Inorganics (Basel) 8 (2020) 40, https://doi.org/10.3390/inorganics8060040.
[21] L. de Castro Alves, S. Yáñez-Vilar, Y. Piñeiro-Redondo, J. Rivas, Novel magnetic nanostructured beads for cadmium(II) removal, Nanomaterials 9 (2019) 356, https://doi.org/10.3390/nano9030356.
[22] S. Azizian, S. Eris, L.D. Wilson, Re-evaluation of the century-old Langmuir isotherm for modeling adsorption phenomena in solution, Chem. Phys. 513 (2018) 99–104, https://doi.org/10.1016/j.chemphys.2018.06.022.
[23] K.Y. Foo, B.H. Hameed, Insights into the modeling of adsorption isotherm systems, Chem. Eng. J. 156 (2010) 2–10, https://doi.org/10.1016/j.cej.2009.09.013.
[24] M. Mozaffari Majd, V. Kordzadeh-Kermani, V. Ghalandari, A. Askari, M. Sillanpää, Adsorption isotherm models: a comprehensive and systematic review (2010−2020), Sci. Total Environ. 812 (2022) 151334, https://doi.org/10.1016/j.scitotenv.2021.151334.
[25] Y.S. Ho, J.F. Porter, G. McKay, Equilibrium isotherm studies for the sorption of divalent metal ions onto peat: copper, nickel and lead single component systems, Water Air Soil Pollut. 141 (2002) 1–33, https://doi.org/10.1023/A:1021304828010.
[26] M. Singh, M. Rayaz, R. Arti, Isotherm and kinetic studies for sorption of Cr(VI) onto Prosopis cineraria leaf powder: a comparison of linear and non-linear regression analysis, Environ. Prog. Sustain. Energy 43 (2024) e14259, https://doi.org/10.1002/EP.14259.
[27] M. Mozaffari Majd, V. Kordzadeh-Kermani, V. Ghalandari, A. Askari, M. Sillanpää, Adsorption isotherm models: a comprehensive and systematic review (2010−2020), Sci. Total Environ. 812 (2022) 151334, https://doi.org/10.1016/J.SCITOTENV.2021.151334.
[28] D. Zhao, J. Feng, Q. Huo, N. Melosh, G.H. Fredrickson, B.F. Chmelka, G.D. Stucky, Triblock copolymer syntheses of mesoporous silica with periodic 50 to 300 angstrom pores, Science 279 (1998) 548–552, https://doi.org/10.1126/science.279.5350.548.
[29] C. Jeon, I.W. Nah, K.-Y. Hwang, Adsorption of heavy metals using magnetically modified alginic acid, Hydrometallurgy 86 (2007) 140–146, https://doi.org/10.1016/j.hydromet.2006.11.010.
[30] J.-L. Gong, X.-Y. Wang, G.-M. Zeng, L. Chen, J.-H. Deng, X.-R. Zhang, Q.-Y. Niu, Copper (II) removal by pectin–iron oxide magnetic nanocomposite adsorbent, Chem. Eng. J. 185–186 (2012) 100–107, https://doi.org/10.1016/j.cej.2012.01.050.
[31] D. Ghahremani, I. Mobasherpour, S.A. Mirhosseini, Sorption Thermodynamic and Kinetic Studies of Lead Removal from Aqueous Solutions by Nano Tricalcium Phosphate, Bulletin de La Société Royale Des Sciences de Liège, 2017, pp. 96–112, https://doi.org/10.25518/0037-9565.7231.
[32] T. Shahwan, H.N. Erten, Thermodynamic parameters of Cs+ sorption on natural clays, J. Radioanal. Nucl. Chem. 253 (2002) 115–120, https://doi.org/10.1023/A:1015824819940.
[33] J.A. García-Calzón, M.E. Díaz-García, Characterization of binding sites in molecularly imprinted polymers, Sensor. Actuator. B Chem. 123 (2007) 1180–1194, https://doi.org/10.1016/J.SNB.2006.10.068.
[34] N. Ayawei, A.N. Ebelegi, D. Wankasi, Modelling and interpretation of adsorption isotherms, J. Chem. 2017 (2017) 1–11, https://doi.org/10.1155/2017/3039817.
[35] I.D. Mall, V.C. Srivastava, N.K. Agarwal, I.M. Mishra, Adsorptive removal of malachite green dye from aqueous solution by bagasse fly ash and activated carbon-kinetic study and equilibrium isotherm analyses, Colloids Surf. A Physicochem. Eng. Asp. 264 (2005) 17–28, https://doi.org/10.1016/j.colsurfa.2005.03.027.
[36] N.A.- Salam, F.A. Ugbe, A.V.I. Ugbe, Optimization and sorption isotherms analysis of anionic dye eosin yellow decontamination by goethite adsorbents, Acta Scientifica Malaysia 4 (2020) 75–81, https://doi.org/10.26480/asm.02.2020.75.81.
[37] G. William Kajjumba, S. Emik, A. Öngen, H. Kurtulus Özcan, S. Aydın, Modelling of adsorption kinetic processes—errors, theory and application, in: Advanced Sorption Process Applications, IntechOpen, 2019, https://doi.org/10.5772/intechopen.80495.
[38] J. López-Luna, et al., Linear and nonlinear kinetic and isotherm adsorption models for arsenic removal by manganese ferrite nanoparticles, SN Appl. Sci. 1 (2019) 950, https://doi.org/10.1007/s42452-019-0977-3.
[39] E.E. Jasper, V.O. Ajibola, J.C. Onwuka, Nonlinear regression analysis of the sorption of crystal violet and methylene blue from aqueous solutions onto an agro-waste derived activated carbon, Appl. Water Sci. 10 (2020) 132, https://doi.org/10.1007/s13201-020-01218-y.
[40] D. Saikia, T.-H. Wang, C.-J. Chou, J. Fang, L.-D. Tsai, H.-M. Kao, A comparative study of ordered mesoporous carbons with different pore structures as anode materials for lithium-ion batteries, RSC Adv. 5 (2015) 42922–42930, https://doi.org/10.1039/C5RA05168A.
[41] K.P. Shwetha, S.G. Divakara, M.K. Sudha Kamath, T. Gupta, Synthesis and electrochemical characterization of mesoporous graphitic carbon nitride for super capacitor applications, Mater. Today Proc. 76 (2023) 219–226, https://doi.org/10.1016/j.matpr.2023.01.049.
[42] K. Quiroz-Estrada, M. Esparza-Schulz, C. Felipe, A better understanding of the SBA-15 pores filling through textural changes in CMK-3 carbon synthesis and its CO2: CH4 adsorption selectivity, J. Composites Sci. 6 (2022) 344, https://doi.org/10.3390/jcs6110344.
[43] H. Daemi, M. Barikani, Synthesis and characterization of calcium alginate nanoparticles, sodium homopolymannuronate salt and its calcium nanoparticles, Sci. Iran. 19 (2012) 2023–2028, https://doi.org/10.1016/j.scient.2012.10.005.
[44] M.A.B.M. Kassim, N.H.M. Kaus, S.S. Imam, S. Sagadevan, S. Salaeh, Rapid and facile chemical synthesis of Fe3O4/biochar nanocomposite for the adsorptive removal of fluoroquinolones from aqueous solution, Inorg. Chem. Commun. 156 (2023) 111156, https://doi.org/10.1016/J.INOCHE.2023.111156.
[45] P.M. Bedê, et al., Nanostructured magnetic alginate composites for biomedical applications, Polímeros 27 (2017) 267–272, https://doi.org/10.1590/0104-1428.2267.
[46] R. Guo, J. Guo, F. Yu, D.D. Gang, Synthesis and surface functional group modifications of ordered mesoporous carbons for resorcinol removal, Microporous Mesoporous Mater. 175 (2013) 141–146, https://doi.org/10.1016/j.micromeso.2013.03.028.
[47] J. Goscianska, M. Marciniak, R. Pietrzak, Mesoporous carbons modified with lanthanum(III) chloride for methyl orange adsorption, Chem. Eng. J. 247 (2014) 258–264, https://doi.org/10.1016/j.cej.2014.03.012.
[48] F. Batool, J. Akbar, S. Iqbal, S. Noreen, S.N.A. Bukhari, Study of isothermal, kinetic, and thermodynamic parameters for adsorption of cadmium: an overview of linear and nonlinear approach and error analysis, Bioinorgan. Chem. Appl. 2018 (2018), https://doi.org/10.1155/2018/3463724.
[49] D.Q. Hung, L.X. Dinh, N. Van Tung, L.T.M. Huong, N.T. Lien, P.T. Minh, T.H. Le, The adsorption kinetic and isotherm studies of metal ions (Co2+, Sr2+, Cs+) on Fe3O4 nanoparticle of radioactive importance, Results Chem. 6 (2023) 101095, https://doi.org/10.1016/J.RECHEM.2023.101095.

[50] M.A. Hossain, H.H. Ngo, W.S. Guo, L.D. Nghiem, F.I. Hai, S. Vigneswaran, T. V. Nguyen, Competitive adsorption of metals on cabbage waste from multi-metal solutions, Bioresour. Technol. 160 (2014) 79–88, https://doi.org/10.1016/j.biortech.2013.12.107.

[51] X. Long, R. Zhang, R. Rong, P. Wu, S. Chen, J. Ao, L. An, Y. Fu, H. Xie, Adsorption characteristics of heavy metals Pb2+ and Zn2+ by magnetic biochar obtained from modified AMD sludge, Toxics 11 (2023), https://doi.org/10.3390/TOXICS11070590.

[52] Z. Gao, T.J. Bandosz, Z. Zhao, M. Han, J. Qiu, Investigation of factors affecting adsorption of transition metals on oxidized carbon nanotubes, J. Hazard Mater. 167 (2009) 357–365, https://doi.org/10.1016/j.jhazmat.2009.01.050.

[53] T. Bohli, A. Ouederni, I. Villaescusa, Simultaneous adsorption behavior of heavy metals onto microporous olive stones activated carbon: analysis of metal interactions, EuroMediterr. J. Environ. Integr. 2 (2017), https://doi.org/10.1007/S41207-017-0030-0.

[54] K.P. Kepp, Thermochemically consistent free energies of hydration for di- and trivalent metal ions, J. Phys. Chem. A 122 (2018) 7464–7471, https://doi.org/10.1021/ACS.JPCA.8B06674.

[55] E. Kokkinos, K. Soukakos, M. Kostoglou, M. Mitrakas, Cadmium, mercury, and nickel adsorption by tetravalent manganese feroxyhyte: selectivity, kinetic modeling, and thermodynamic study, Environ. Sci. Pollut. Control Ser. 25 (2018) 12263–12273, https://doi.org/10.1007/S11356-017-9738-2.

[56] R.N. Jones, D.A. Ramsay, D.S. Keir, K. Dobriner, The intensities of carbonyl bands in the infrared spectra of steroids [1], J. Am. Chem. Soc. 74 (1952) 80–88, https://doi.org/10.1021/ja01121a019.